

3D quaternionic condensations, Hopf invariants, and skyrmion lattices with synthetic spin-orbit coupling

Yi Li,^{1,2} Xiangfa Zhou,³ and Congjun Wu¹

¹*Department of Physics, University of California, San Diego, La Jolla, California 92093, USA*

²*Princeton Center for Theoretical Science, Princeton University, Princeton, NJ 08544*

³*Key Laboratory of Quantum Information, University of Science and Technology of China, CAS, Hefei, Anhui 230026, China*

We study the topological configurations of the two-component condensates of bosons with the 3D $\vec{\sigma} \cdot \vec{p}$ Weyl-type spin-orbit coupling subject to a harmonic trapping potential. The topology of the condensate wavefunctions manifests in the quaternionic representation. In comparison to the $U(1)$ complex phase, the quaternionic phase manifold is S^3 and the spin orientations form the S^2 Bloch sphere through the 1st Hopf mapping. The spatial distributions of the quaternionic phases exhibit the 3D skyrmion configurations, and the spin distributions possess non-trivial Hopf invariants. Spin textures evolve from the concentric distributions at the weak spin-orbit coupling regime to the rotation symmetry breaking patterns at the intermediate spin-orbit coupling regime. In the strong spin-orbit coupling regime, the single-particle spectra exhibit the Landau-level type quantization. In this regime, the three-dimensional skyrmion lattice structures are formed when interactions are below the energy scale of Landau level mixings. Sufficiently strong interactions can change condensates into spin-polarized plane-wave states, or, superpositions of two plane-waves exhibiting helical spin spirals.

PACS numbers: 03.75.Mn, 03.75.Lm, 03.75.Nt, 67.85.Fg

I. INTRODUCTION

Quantum mechanical wavefunctions generally speaking are complex-valued. However, for the single component boson systems, their ground state many-body wavefunctions are highly constrained, which are usually positive-definite [1], as a consequence of the Perron-Frobenius theorem in the mathematical context of matrix analysis [2]. This is a generalization of the “no-node” theorem of the single-particle quantum mechanics, for example, both the ground state wavefunctions of harmonic oscillators and hydrogen atoms are nodeless. Although the positive-definiteness does not apply to the many-body fermion wavefunctions because Fermi statistics necessarily leads to nodal structures, it remains valid for many-body boson systems. It applies under the following conditions: the Laplacian type kinetic energy, the arbitrary single-particle potential, and the coordinate-dependent interactions. The positive-definiteness of the ground state wavefunctions implies that time-reversal (TR) symmetry cannot be spontaneously broken in conventional Bose-Einstein condensates (BEC), such as the superfluid ^4He and most ground state BECs of ultra-cold alkali bosons [3].

It would be interesting to seek unconventional BECs beyond the constraint of positive-definite condensate wavefunctions [4]. The spin-orbit coupled boson systems are an ideal platform to study this class of exotic states of bosons, which can spontaneously breaking the TR symmetry. In addition to a simple Laplacian, the kinetic energy contains the spin-orbit coupling term linearly dependent on momentum. If the bare interaction is spin-independent, the condensate wavefunctions are heavily degenerate. An “order-from-disorder” calculation based on the zero-point energy of the Bogoliubov spectra was

perform to select the condensate configuration [4]. Inside the harmonic trap, it is predicted that the condensates spontaneously develop the half-quantum vortex coexisting with 2D skyrmion-type spin textures [5]. Experimentally, spin-orbit coupled bosons have been realized in exciton systems in semi-conducting quantum wells. Spin texture configurations similar to those predicted in Ref. [5] have been observed [6]. On the other hand, the progress of synthetic artificial gauge fields in ultra-cold atomic gases greatly stimulates the investigation of the above exotic states of bosons [7, 8]. Extensive studies have been performed for bosons with the 2D Rashba spin-orbit coupling, which exhibit various spin structures arising from the competitions among the spin-orbit coupling, interaction, and the confining trap energy [5, 9–16].

Most studies so far have been on the two-dimensional spin-orbit coupled bosons. It would be interesting to further consider the unconventional condensates of bosons with the three-dimensional Weyl-type spin-orbit coupling, whose experimental realization has been proposed by the authors through atom-light interactions in a combined tripod and tetrapod level system [20] and also by Anderson *et al.* [21]. As will be shown below, the quaternion representation provides a natural and most beautiful description of the topological condensation configurations. Quaternions are an extension of complex numbers as the first discovered non-commutative division algebra, which has provided a new formulation of quantum mechanics [17–19]. Similarly to complex numbers whose phases span a unit circle S^1 , the quaternionic phases span a three dimensional unit sphere S^3 . The spin distributions associated with quaternionic wavefunctions are obtained through the 1st Hopf map $S^3 \rightarrow S^2$ as will be explained below. It would be interesting to search for BECs with non-trivial topological defects associated with

the quaternionic phase structure. It will be a new class of unconventional BECs beyond the “no-node” theorem breaking TR symmetry spontaneously.

In this article, we consider the unconventional condensate wavefunctions with the 3D Weyl-type spin-orbit coupling $\vec{\sigma} \cdot \vec{p}$. The condensation wavefunctions exhibit topologically non-trivial configurations as 3D skyrmions, and spin density distributions are also non-trivial with non-zero Hopf invariants. These topological configurations can be best represented as defects of quaternion phase distributions. Spatial distributions of the quaternionic phase textures and spin textures are concentric at weak spin-orbit couplings. As increasing spin-orbit coupling, these textures evolve to lattice structures which are the 3D quaternionic analogy of the 2D Abrikosov lattice of the usual complex condensate.

The rest part of this article is organized as follows. In Sect. II, we define the model Hamiltonian. In Sect. III, the condensate wavefunctions in the weak spin-orbit regime are studied. Topological analyses on the skyrmion configurations and Hopf invariants are performed by using the quaternion representation. In Sect. IV, the skyrmion lattice configuration of the spin textures is studied in the intermediate and strong spin-orbit coupling regimes. In Sect. V, superpositions of plane-wave condensate configurations are studied. Conclusions are made in Sect. VI.

II. THE MODEL HAMILTONIAN

We consider a two-component boson system with the 3D spin-orbit coupling of the $\vec{\sigma} \cdot \vec{p}$ -type confined in a harmonic trap. The free part of the Hamiltonian is defined as

$$H_0 = \int d^3\vec{r} \psi_\gamma^\dagger(\vec{r}) \left\{ -\frac{\hbar^2 \vec{\nabla}^2}{2m} + i\hbar\lambda \vec{\sigma}_\gamma \cdot (\vec{\nabla}) \right. \\ \left. + \frac{1}{2}m\omega^2 \vec{r}^2 \right\} \psi_\delta(\vec{r}), \quad (1)$$

where γ and δ equal \uparrow and \downarrow referring to two internal states of bosons; $\vec{\sigma}$ are Pauli matrices; m is the boson mass; λ is the spin-orbit coupling strength with the unit of velocity; ω is the trap frequency. At the single-particle level, Eq. (1) satisfies the Kramer-type time-reversal symmetry of $T = (-i\sigma_2)C$ with the property of $T^2 = -1$. However, parity is broken by spin-orbit coupling. In the absence of the trap, good quantum numbers for the single-particle states are the eigenvalues ± 1 of helicity $\vec{\sigma} \cdot \vec{p}/|p|$, where p is the momentum. This results in two branches of dispersions

$$\epsilon_\pm(\vec{k}) = \frac{\hbar^2}{2m}(k \mp k_{so})^2, \quad (2)$$

where $\hbar k_{so} = m\lambda$. The lowest single-particle energy states lie in the sphere with the radius k_{so} denoted as the spin-orbit sphere. It corresponds to a spin-orbit length

scale $l_{so} = 1/k_{so}$ in real space. The harmonic trap has a natural length scale $l_T = \sqrt{\frac{\hbar}{m\omega}}$, and thus the dimensionless parameter $\alpha = l_T k_{so}$ describes the relative spin-orbit coupling strength.

As for the interaction Hamiltonian, we use the contact s -wave scattering interaction defined as

$$H_{int} = \frac{g_{\gamma\delta}}{2} \int d^3\vec{r} \psi_\gamma^\dagger(\vec{r}) \psi_\delta^\dagger(\vec{r}) \psi_\delta(\vec{r}) \psi_\gamma(\vec{r}). \quad (3)$$

Two different interaction parameters are allowed, including the intra and inter-component ones defined as $g_{\uparrow\uparrow} = g_{\downarrow\downarrow} = g$, and $g_{\uparrow\downarrow} = cg$, where c is a constant.

In the previous study of the 2D Rashba spin-orbit coupling with harmonic potentials [5, 15], the single-particle eigenstates are intuitively expressed in the momentum representation: the low energy state lies around a ring in momentum space, and the harmonic potential becomes the planar rotor operator on this ring subject to a π -flux, which quantizes the angular momentum j_z to half integers. Similar picture also applies in 3D [5, 22]. The low energy states are around the spin-orbit sphere. In the projected low energy Hilbert space, the eigenvectors read

$$\psi_+(\vec{k}) = (\cos \frac{\theta_k}{2}, \sin \frac{\theta_k}{2} e^{i\phi_k})^T. \quad (4)$$

The harmonic potential is again a rotor Hamiltonian on the spin-orbit sphere subject to the Berry gauge connection as

$$V_{tp} = \frac{1}{2}m(i\nabla_k - \vec{A}_k)^2 \quad (5)$$

with the moment of inertial $I = M_k k_{so}^2$ and $M_k = \hbar^2/(m\omega^2)$. $\vec{A}_k = i\langle\psi_+(\vec{k})|\nabla_k|\psi_+(\vec{k})\rangle$ is the vector potential of a $U(1)$ magnetic monopole, which quantizes the angular momentum j to half-integers. While the radial energy is still quantized in terms of $\hbar\omega$, the angular energy dispersion with respect to j is strongly suppressed at large values of α as

$$E_{n_r, j, j_z} \approx \left(n_r + \frac{j(j+1)}{2\alpha^2}\right)\hbar\omega + \text{const}, \quad (6)$$

where n_r is the radial quantum number. As further shown in Ref. [20], in the case $\alpha \gg 1$, all the states with the same n_r but different j and j_z are nearly degenerate, thus can be viewed as one 3D Landau level with spherical symmetry but the broken parity. If filled with fermions, the system belongs to the Z_2 -class of 3D strong topological insulators.

Now we load the system with bosons. The interaction energy scale is defined as $E_{int} = gN_0/l_T^3$, where N_0 is the total particle number in the condensate. The corresponding dimensionless parameter is $\beta = E_{int}/\hbar\omega$. At the Hartree-Fock level, the Gross-Pitaevskii energy functional is defined in terms of the condensate wavefunction

$\Psi = (\Psi_\uparrow, \Psi_\downarrow)^T$ as

$$E = \int d^3\vec{r} (\Psi_\uparrow^\dagger, \Psi_\downarrow^\dagger) \left\{ -\frac{\hbar^2 \nabla^2}{2m} - i\lambda \hbar \vec{\nabla} \cdot \vec{\sigma} + \frac{1}{2} m \omega^2 r^2 \right. \\ \left. + g \begin{pmatrix} n_\uparrow + c n_\downarrow & 0 \\ 0 & c n_\uparrow + n_\downarrow \end{pmatrix} \right\} \begin{pmatrix} \Psi_\uparrow \\ \Psi_\downarrow \end{pmatrix}, \quad (7)$$

where $n_{\uparrow,\downarrow}(\vec{r}) = N_0 |\Psi_{\uparrow,\downarrow}(\vec{r})|^2$ are the particle densities of two components, respectively, and $\Psi(\vec{r})$ is normalized as $\int d^3\vec{r} \Psi^\dagger(\vec{r}) \Psi(\vec{r}) = 1$. The condensate wavefunction $\Psi(\vec{r})$ is solved numerically by using the standard method of imaginary time evolution. The dimensionless form of the Gross-Pitaevskii equation is

$$E' = \int d^3\vec{r}' (\tilde{\Psi}_\uparrow^\dagger, \tilde{\Psi}_\downarrow^\dagger) \left\{ -\frac{\tilde{\nabla}'^2}{2} - i\alpha \tilde{\nabla}' \cdot \vec{\sigma} + \frac{r'^2}{2} \right. \\ \left. + \beta \begin{pmatrix} \tilde{n}_\uparrow + c \tilde{n}_\downarrow & 0 \\ 0 & c \tilde{n}_\uparrow + \tilde{n}_\downarrow \end{pmatrix} \right\} \begin{pmatrix} \tilde{\Psi}_\uparrow \\ \tilde{\Psi}_\downarrow \end{pmatrix}, \quad (8)$$

where $E' = E/(\hbar\omega)$, $\tilde{\nabla}' = l_T \vec{\nabla}$; $\vec{r}' = \vec{r}/l_T$; $\tilde{\Psi}_\uparrow$ and $\tilde{\Psi}_\downarrow$ are the renormalized condensate wavefunctions satisfying $\int d^3\vec{r}' |\tilde{\Psi}_\uparrow|^2 + |\tilde{\Psi}_\downarrow|^2 = 1$; $\tilde{n}_\uparrow = |\tilde{\Psi}_\uparrow|^2$ and $\tilde{n}_\downarrow = |\tilde{\Psi}_\downarrow|^2$.

III. THE WEAK SPIN-ORBIT COUPLING REGIME

In this section, we consider the condensate configuration in the limit of weak spin-orbit coupling, say, $\alpha \sim 1$. In this regime, the single-particle spectra still resemble those of the harmonic trap. We study the case that interactions are not strong enough to mix states with different angular momenta.

A. The spin-orbit coupled condensate

In this regime, the condensate wavefunction Ψ remains the same symmetry structure as the single-particle wavefunction over a wide range of interaction parameter β , i.e., Ψ remains the eigenstates of $j = \frac{1}{2}$ as confirmed numerically below. Ψ can be represented as

$$\Psi_{j=j_z=\frac{1}{2}}(r, \hat{\Omega}) = f(r) Y_{j,j_z}^+(\hat{\Omega}) + i g(r) Y_{j,j_z}^-(\hat{\Omega}), \quad (9)$$

where $f(r)$ and $g(r)$ are real radial functions. $Y_{j,j_z}^\pm(\hat{\Omega})$ are the spin-orbit coupled spherical harmonic functions with even and odd parities, respectively. For example, for the case of $j = j_z = \frac{1}{2}$, they are

$$Y_{\frac{1}{2},\frac{1}{2}}^+(r, \hat{\Omega}) = \begin{pmatrix} 1 \\ 0 \end{pmatrix}, \quad Y_{\frac{1}{2},\frac{1}{2}}^-(r, \hat{\Omega}) = \begin{pmatrix} \cos \theta \\ \sin \theta e^{i\phi} \end{pmatrix}, \quad (10)$$

whose orbital partial-wave components are s and p -wave, respectively. The TR partner of Eq. (9) is $\psi_{j_z=-\frac{1}{2}} = \hat{T} \psi_{j_z=\frac{1}{2}} = i \sigma_2 \psi_{j_z=\frac{1}{2}}^*$. The two terms in Eq. (9) are of opposite parity eigenvalues, mixed by the parity

breaking spin-orbit coupling $\vec{\sigma} \cdot \vec{p}$. The coefficient i of the Y_{j,j_z}^- term is because the matrix element $\langle Y_{j,j_z}^+ | \vec{\sigma} \cdot \vec{p} | Y_{j,j_z}^- \rangle$ is purely imaginary.

For the non-interacting case, the radial wavefunctions up to a Gaussian factor can be approximated by spherical Bessel functions as

$$f(r) \approx j_0(k_{so} r) e^{-r^2/2l_T^2}, \quad g(r) \approx j_1(k_{so} r) e^{-r^2/2l_T^2}, \quad (11)$$

which correspond to the s and p -partial waves, respectively. Both of them oscillate along the radial direction and the pitch values are around k_{so} . At $r = 0$, $f(r)$ reaches the maximum and $g(r)$ is 0. As r increases, roughly speaking, the zero points of $f(r)$ corresponds to the extrema of $g(r)$ and vice versa. Repulsive interactions expand the spatial distributions of $f(r)$ and $g(r)$, but the above picture still holds qualitatively. In other words, there is a $\frac{\pi}{2}$ -phase shift between the oscillations of $f(r)$ and $g(r)$.

B. The quaternion representation

Can we have unconventional BECs with non-trivial quaternionic condensate wavefunctions? Actually, the topological structure of condensate wavefunction Eq. (9) manifests clearly in the quaternion representation as shown below.

We define the following mapping from the complex two-component vector $\Psi = (\Psi_\uparrow, \Psi_\downarrow)^T$ to a quaternion variable through

$$\xi = \xi_0 + \xi_1 i + \xi_2 j + \xi_3 k, \quad (12)$$

where

$$\xi_0 = \text{Re} \Psi_\uparrow, \xi_1 = \text{Im} \Psi_\downarrow, \xi_2 = -\text{Re} \Psi_\downarrow, \xi_3 = \text{Im} \Psi_\uparrow. \quad (13)$$

i, j, k are the imaginary units satisfying $i^2 = j^2 = k^2 = -1$, and the anti-commutation relation $ij = -ji = k$. The TR transformation on ξ is just $-\bar{j}\xi$.

Eq. (9) can be expressed in the quaternionic exponential form as

$$\xi_{j=j_z=\frac{1}{2}}(r, \hat{\Omega}) = |\xi(r)| e^{\vec{\omega}(\hat{\Omega}) \gamma(r)} = |\xi| (\cos \gamma + \vec{\omega} \sin \gamma), \quad (14)$$

where

$$|\xi(r)| = [f^2(r) + g^2(r)]^{\frac{1}{2}}, \\ \vec{\omega}(\hat{\Omega}) = \sin \theta \cos \phi i + \sin \theta \sin \phi j + \cos \theta k, \\ \cos \gamma(r) = f(r)/|\xi(r)|, \quad \sin \gamma(r) = g(r)/|\xi(r)|. \quad (15)$$

$\omega(\hat{\Omega})$ is the imaginary unit along the direction of $\hat{\Omega}$ satisfying $\vec{\omega}^2(\hat{\Omega}) = -1$. According to the oscillating properties of $f(r)$ and $g(r)$, $\gamma(r)$ spirals as r increases. At the n -th zero point of $g(r)$ denoted r_n , $\gamma(r_n) = n\pi$ where $n \geq 0$ and we define $r_0 = 0$, while at the n -th zero point of $f(r)$ denoted r'_n , $\gamma(r'_n) = (n - \frac{1}{2})\pi$ where $n \geq 1$.

In 3D, the condensate wavefunctions can be topologically non-trivial because the homotopy group of the

quaternionic phase is $\pi_3(S^3) = Z$ [23, 24]. The corresponding winding number, i.e. the Pontryagin index, of the mapping $S^3 \rightarrow S^3$ is the 3D skyrmion number. The spatial distribution of the quaternionic phase $e^{\tilde{\omega}(\hat{\Omega})\gamma(r)}$ defined in Eq. 14, which lies on S^3 , exhibits a topologically nontrivial mapping from R^3 to S^3 , i.e., a 3D multiple skyrmion configuration. This type of topological defects are non-singular which is different from the usual vortex in single component BEC. In realistic trapping systems, the coordinate space is the open R^3 . At large distance $r \gg l_T$, $|\xi(r)|$ decays exponentially, where the quaternionic phase and the mapping are not well-

defined. Nevertheless, in each concentric spherical shell with $r_n < r < r_{n+1}$, $\gamma(r)$ winds from $n\pi$ to $(n+1)\pi$, and $\omega(\hat{\Omega})$ covers all the directions, thus this shell contributes 1 to the winding number of $e^{\tilde{\omega}(\hat{\Omega})\gamma(r)}$ on S^3 . If the system size is truncated at the order of l_T , the skyrmion number can be approximated at the order of $l_T k_{so} = \alpha$.

There exists an interesting difference from the previously studied 2D case: Although the spin density distribution exhibit the 2D skyrmion configuration due to $\pi_2(S^2)$ [5, 15, 16], the 2D condensation wavefunctions have no well-defined topology due to $\pi_2(S^3) = 0$.

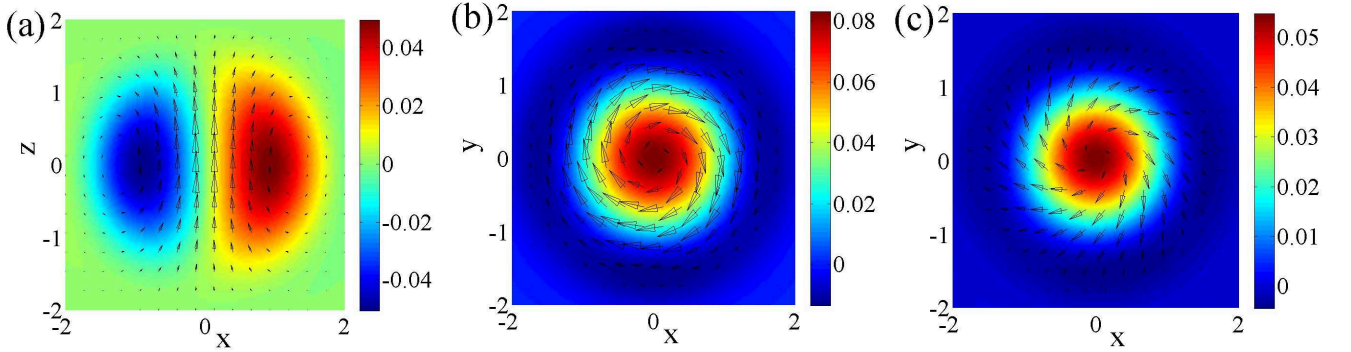


FIG. 1: The distribution of $\tilde{S}(\vec{r})$ in a) the xz -plane and in the horizontal planes with b) $z = 0$ and c) $z/l_T = \frac{1}{2}$. The unit length is set as $l_T = 1$ in all the figures in this article. The color scale shows the magnitude of out-plane component S_y in a) and S_z in b) and c). The parameter values are $\alpha = 1.5$, $c = 1$, and $\beta = 30$, and the length unit in these and all the figures below is l_T .

C. The Hopf mapping and Hopf invariant

Exotic spin textures in spinor condensates have been extensively investigated [25–27]. In our case, the 3D spin density distributions $\tilde{S}(\vec{r})$ exhibit a novel configuration with non-trivial Hopf invariants due to the non-trivial homotopy group $\pi_3(S^2) = Z$ [23, 24]. $\tilde{S}(\vec{r})$ can be obtained from $\xi(r)$ through the 1st Hopf map defined as $\tilde{S}(\vec{r}) = \frac{1}{2}\psi^\dagger_\gamma \vec{\sigma}_{\gamma\beta} \psi_\beta$, or, in the quaternionic representation,

$$\frac{1}{2}\bar{\xi}k\xi = S_x i + S_y j + S_z k, \quad (16)$$

where $\bar{\xi} = \xi_0 - \xi_1 i - \xi_2 j - \xi_3 k$ is the quaternionic conjugate of ξ . The Hopf invariant of the 1st Hopf map is just 1 [24]. The real space concentric spherical shell $r_n < r < r_{n+1}$ maps to the quaternionic phase S^3 , and the latter further maps to the S^2 Bloch sphere through the 1st Hopf map. The winding number of the first map is 1, and the Hopf invariant of the second map is also 1, thus the Hopf invariant of the shell $r_n < r < r_{n+1}$ to S^2 is 1. Rigorously speaking, the magnitude of $\tilde{S}(\vec{r})$ decays exponentially at $r \gg l_T$, and thus the total Hopf invariant is not well-defined in the open R^3 space. Again, if we truncate the

system size at l_T , the Hopf invariant is approximately at the order of α .

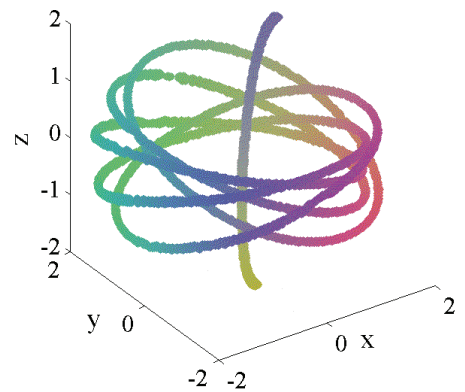


FIG. 2: The Hopf fibration of the spin texture configuration in Fig. 1. Every circle represents a spin orientation, and every two circles are linked with the linking number 1.

Next we present numeric results for the spin textures associated with the condensation wavefunction Eq. 9 as

plotted in Fig. 1. Explicitly, $\vec{S}(\vec{r})$ is expressed as

$$\begin{aligned} \begin{bmatrix} S_x(\vec{r}) \\ S_y(\vec{r}) \end{bmatrix} &= g(r) \sin \theta \begin{bmatrix} \cos \phi & -\sin \phi \\ \sin \phi & \cos \phi \end{bmatrix} \begin{bmatrix} g(r) \cos \theta \\ f(r) \end{bmatrix}, \\ S_z(\vec{r}) &= f^2(r) + g^2(r) \cos 2\theta, \end{aligned} \quad (17)$$

In the xz -plane, the in-plane components S_x and S_z form a vortex in the half plane of $x > 0$ and S_y is prominent in the core. The contribution at large distance is neglected, where $\vec{S}(\vec{r})$ decays exponentially. Due to the axial symmetry of $\vec{S}(\vec{r})$ in Eq. 17, the 3D distribution is just a rotation of that in Fig. 1 a) around the z -axis. In the xy -plane, spin distribution exhibits a 2D skyrmion pattern, whose in-plane components are along the tangential direction. As the horizontal cross-section shifted along the z -axis, $\vec{S}(\vec{r})$ remains 2D skyrmion-like, but its in-plane components are twisted around the z -axis. The spin configuration at $z = -z_0$ can be obtained by a com-

bined operation of TR and rotation around the y -axis 180° , thus its in-plane components are twisted in an opposite way compared to those at $z = z_0$. Combining the configurations on the vertical and horizontal cross sections, we complete the 3D distribution of $\vec{S}(\vec{r})$ with non-zero Hopf invariant.

The non-trivial structure of the Hopf invariant of the above spin configuration can be revealed by plotting its Hopf fibration in terms of the linked non-crossing circles in real space, as shown in Fig. 2. For all the points on each circle, their normalized spin polarizations $\langle \vec{\sigma} \rangle / |\langle \vec{\sigma} \rangle|$ are the same, corresponding to a single point on the S^2 sphere. In addition, every two circles are linked with each other with the linking number 1, which is the standard Hopf bundle structure describing a many-to-one map from S^3 to S^2 . Ultracold bosons with synthetic spin-orbit coupling provide a novel platform to study such beautiful mathematical ideas in realistic physics systems.

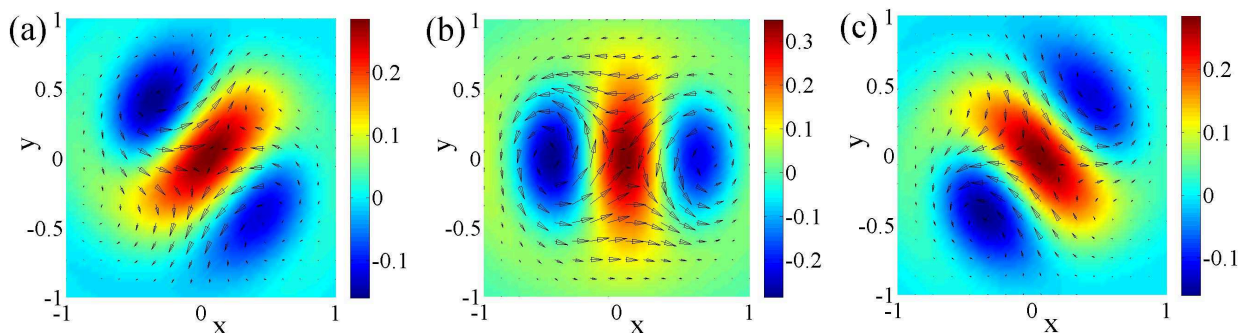


FIG. 3: The distribution of $\vec{S}(\vec{r})$ in horizontal cross-sections with a) $z/l_T = -0.5$, b) $z/l_T = 0$, c) $z/l_T = 0.5$, respectively. The color scale shows the value of S_z , and parameter values are $\alpha = 4$, $\beta = 2$, and $c = 1$.

IV. THE INTERMEDIATE AND STRONG SPIN-ORBIT COUPLING REGIME

A. The intermediate spin-orbit coupling strength

Next we consider the case of the intermediate spin-orbit coupling strength, i.e., $1 < \alpha < 10$, at which the single-particle spectra evolve from the case of the harmonic potential to Landau level-like as shown in Eq. 6. Interactions are sufficiently strong to mix a few lowest energy states with different angular momenta j . As a result, rotational symmetry is broken and complex patterns appear.

In this case, the topology of condensate wavefunctions is still 3D skyrmion-like mapping from R^3 to S^3 , and spin textures with the non-trivial Hopf invariant are obtained through the 1st Hopf map. Compared to the weak spin-orbit coupling case, the quaternionic phase skyrmions and spin textures are no longer concentric, but split to a multi-centered pattern. The numeric results of $\vec{S}(\vec{r})$ are

plotted in Fig. 3 for different horizontal cross-sections. In the xy -plane, \vec{S} exhibits the 2D skyrmion pattern as shown in Fig. 3 (b): The in-plane components form two vortices and one anti-vortex, while S_z 's inside the vortex and anti-vortex cores are opposite in direction, thus they contribute to the skyrmion number with the same sign. The spin configuration at $z = z_0 > 0$ is shown in Fig. 3 (a), which is twisted around the z -axis clock-wise. After performing the combined TR and rotation around the y -axis 180° , we arrive at the configuration at $z = -z_0$ in Fig. 3(b).

B. The strong spin-orbit coupling regime

We next consider the case of strong spin-orbit coupling, i.e., $\alpha \gg 1$. The single-particle spectra already exhibit the Landau-level type quantization in this regime as shown in Eq. 6. The single-particle eigenstates with $n_r = 0$ are nearly degenerate i.e., they form the low-

est Landau level states. We assume that the interaction strength is enough to mix states inside the lowest Landau level but is still relatively weak not to induce inter-Landau level mixing.

In this regime, the length scale of each skyrmion is shortened as enlarging the spin-orbit coupling strength. As we can imagine, more and more skyrmions appear and will form a 3D lattice structure, which is the SU(2) generalization of the 2D Abrikosov lattice of the usual U(1) superfluid. We have numerically solved the Gross-Pitaevskii equation Eq. 7 and found the lattice structure: Each lattice site is a single skyrmion of the condensate wavefunction $\xi(\vec{r})$, whose spin configuration exhibits the texture configuration approximately with a unit Hopf invariant. The numeric results for the spin texture configuration

are depicted in Fig. 4 a) and b) for two different horizontal cross sections parallel to the xy -plane. In each cross section, spin textures form a square lattice, and the lattice constant d is estimated approximately the spin-orbit length scale as

$$d \simeq 2\pi l_{so} = 2\pi l_T / \alpha. \quad (18)$$

For two horizontal cross sections with a distance of $\Delta z \simeq d/2$, their square lattice configurations are displaced along the diagonal direction: The sites at one layer sit above the plaquette centers of the adjacent layer. As a result, the overall three-dimensional configuration of the topological defects is a body-centered cubic (*bcc*) lattice, and its size is finite confined by the trap.

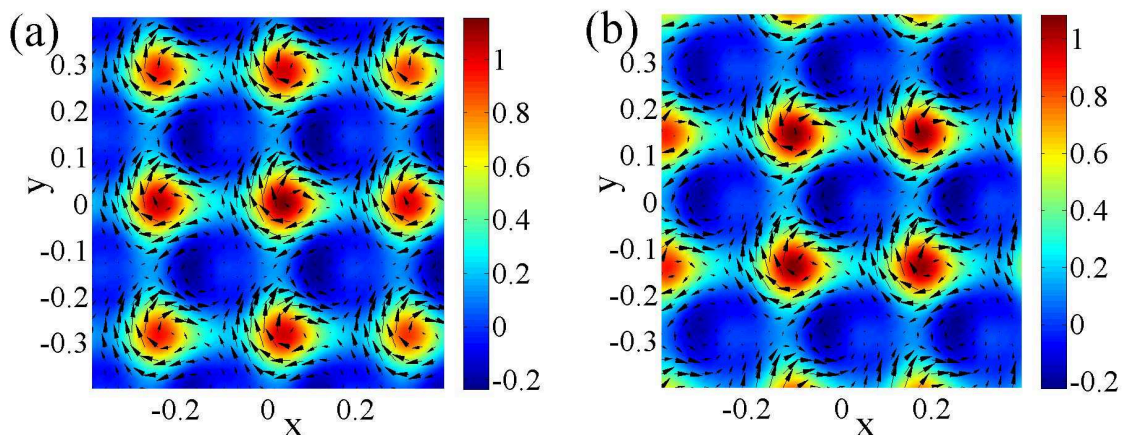


FIG. 4: The distribution of $\vec{S}(\vec{r})$ in horizontal cross-sections with (a) $z/l_T = 0$, (b) $z/l_T = 0.2$, respectively. The color scale shows the value of S_z and parameter values are $\alpha = 22$, $\beta = 1$, and $c = 1$. The overall lattice exhibits the bcc structure.

V. THE EFFECT OF STRONG INTERACTIONS

In this section, we present the condensate configurations in the case that both spin-orbit coupling and interactions are strong, such that different Landau levels are mixed by interactions.

In this case, the effect of the harmonic trapping potential becomes weak compared with interaction energies, thus we can approximate the condensate wavefunctions as superpositions of plane-wave states. The plane-wave components are located on the spin-orbit sphere and the condensate wavefunctions are no longer topological. At $c = 1$, the interaction is spin-independent, and bosons select a superposition of a pair of states $\pm k$ on the spin-orbit sphere, say, $\pm k_{so}\hat{z}$. The condensate wavefunction is written as

$$\psi(\vec{r}) = \sqrt{\frac{N_a}{N_0}} e^{ik_{so}z} |\uparrow\rangle + \sqrt{\frac{N_b}{N_0}} e^{-ik_{so}z} |\downarrow\rangle, \quad (19)$$

with $N_a + N_b = N_0$. The density of Eq. 19 in real space is uniform to minimize the interaction energy at the Hartree-Fock level. However, all the different partitions of $N_{a,b}$ yield the same Hartree-Fock energy. The quantum zero point energy from the Bogoliubov modes removes this accidental degeneracy through the “order-from-disorder” mechanism, which selects the equal partition $N_a = N_b$. The calculation is in parallel to that of the 2D Rashba case performed in Ref. [5], thus will not be presented here. In this case, the condensate is a spin helix propagates along z -axis and spin spirals in the xy -plane.

At $c \neq 1$, the spin-dependent part of the interaction can be written as

$$H_{sp} = \frac{1-c}{2} g \int d^3r (\psi_{\uparrow}^\dagger \psi_{\uparrow} - \psi_{\downarrow}^\dagger \psi_{\downarrow})^2. \quad (20)$$

At $c > 1$, the interaction energy at Hartree-Fock level is minimized for the condensate wavefunction of a plane wave state $e^{ik_{so}z} |\uparrow\rangle$, or, its TR partner.

For $c < 1$, $\langle H_{sp} \rangle$ is minimized if $\langle S_z \rangle = 0$ in space. At the Hartree-Fock level, the condensate can either be a plane-wave state with momentum lying in the equator of the spin-orbit sphere and spin polarizing in the xy -plane, or, the spin spiral state described by Eq. 19 with $N_a = N_b$. An “order-from-disorder” analysis on the Bogoliubov zero-point energies indicates that the spin spiral state

is selected. We also present the numerical results for Eq. (4) in the main text with a harmonic trap in Fig. 5 for the case of $c < 1$. The condensate momenta of two spin components have opposite signs, thus the trap inhomogeneity already prefers the spin spiral state Eq. 19 at the Hartree-Fock level.

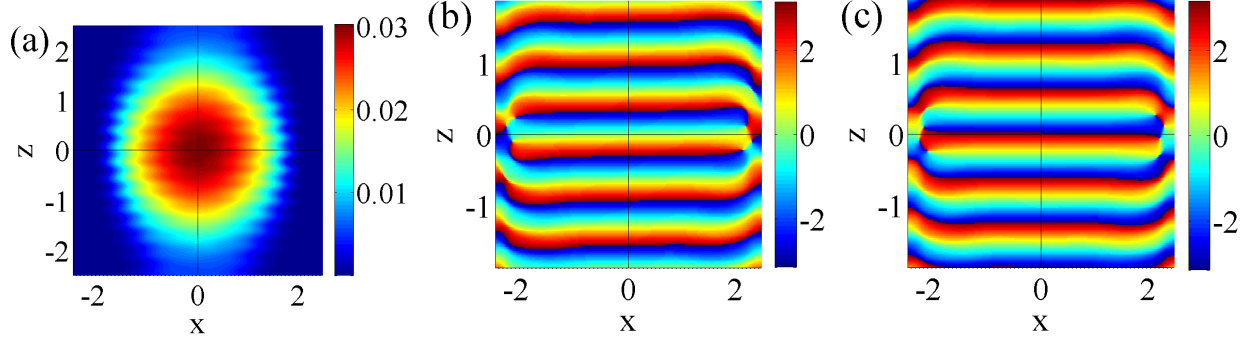


FIG. 5: The density profile (a) for \uparrow -component, and that for \downarrow -component is the same. Phase profiles for (b) \uparrow and (c) \downarrow - components, respectively. Parameter values are $a = 10$, $\beta = 50$, and $c = 0.5$.

VI. CONCLUSION

In summary, we have investigated the two-component unconventional BECs driven by the 3D spin-orbit coupling. In the quaternionic representation, the quaternionic phase distributions exhibit non-trivial 3D skyrmion configurations from R^3 to S^3 . The spin orientation distributions exhibit texture configurations characterized by non-zero Hopf invariants from R^3 to S^2 . These two topological structures are connected through the 1st Hopf map from S^3 to S^2 . At large spin-orbit coupling strength, the crystalline order of spin textures, or, wavefunction skyrmions, are formed, which can be viewed as a generalization of the Abrikosov lattice in 3D.

Note added.— Near the completion of this manuscript, we became aware of a related work by Kawakami *et al.*

[28], in which the condensate wavefunction in the weak spin-orbit coupling case was studied.

Acknowledgments.— Y.L. thanks the Princeton Center for Theoretical Science at Princeton University for support. X. F. Z. acknowledges the support of NFRP (2011CB921204, 2011CBA00200), the Strategic Priority Research Program of the Chinese Academy of Sciences (Grant No. XDB01030000), NSFC (11004186, 11474266), and the Major Research plan of the National Natural Science Foundation of China (91536219). C. W. is supported by the NSF DMR-1410375 and AFOSR FA9550-14-1-0168. C. W. acknowledges the support from the Presidents Research Catalyst Awards of University of California, and National Natural Science Foundation of China (11328403).

-
- [1] R. P. Feynman, *Statistical Mechanics, A Set of Lectures* (Berlin: Addison-Wesley, 1972).
 - [2] R. B. Bapat and T. Raghavan, *Non-Negative Matrices and Applications* (Cambridge University Press, Cambridge, United Kingdom, 1997).
 - [3] A. J. Leggett, Rev. Mod. Phys. **73**, 307 (2001).
 - [4] C. Wu, Mod. Phys. Lett. **23**, 1 (2009).
 - [5] C. Wu, I. Mondragon-Shem, arXiv:0809.3532; C. Wu, I. Mondragon-Shem, and X. F. Zhou, Chin. Phys. Lett., **28**, 097102 (2011).
 - [6] A.A. High *et al.*, Nature **483**, 584 (2012). A.A. High *et al.*, arXiv:1103.0321.
 - [7] Y.-J. Lin *et al.*, Nature **462**, 628 (2009).
 - [8] Y.-J. Lin *et al.*, Nature **471**, 83 (2011).
 - [9] T. Stanescu *et al.*, Phys. Rev. A **78**, 023616 (2008).
 - [10] T.-L. Ho *et al.*, Phys. Rev. Lett. **107**, 150403 (2011).
 - [11] C. Wang *et al.*, Phys. Rev. Lett. **105**, 160403 (2010).
 - [12] S.-K. Yip, Phys. Rev. A **83**, 043616 (2011).
 - [13] Y. Zhang *et al.*, Phys. Rev. Lett. **108**, 035302 (2012).
 - [14] X.-F. Zhou *et al.*, Phys. Rev. A **84**, 063624 (2011).
 - [15] H. Hu *et al.*, Phys. Rev. Lett. **108**, 010402 (2012).
 - [16] S. Sinha, R. Nath, and L. Santos, arXiv:1109.2045.
 - [17] A. V. Balatsky, cond-mat/9205006.
 - [18] S. L. Adler, *Quaternionic Quantum Mechanics and Quantum Fields* (Oxford University Press, Oxford, 1995).
 - [19] D. Finkelstein *et al.*, J. Math. Phys. (N. Y.) **3**, 207 (1962).

- [20] Y. Li *et al.*, Phys. Rev. B **85**, 125122 (2012).
- [21] B. M. Anderson *et al.*, arXiv:1112.6022.
- [22] S. K. Ghosh *et al.*, Phys. Rev. A, **84**, 053629 (2011).
- [23] F. Wilczek and A. Zee, Phys. Rev. Lett. **51**, 2250 (1983).
- [24] M. Nakahara, *Geometry, topology, and physics*, (Taylor & Francis, 2003)
- [25] F. Zhou, Int. J. Mod. Phys. B **17**, 2643-2698 (2003); E. Demler and F. Zhou, Phys. Rev. Lett. **88**, 163001 (2002).
G. W. Semenoff and F. Zhou, Phys. Rev. Lett. **98**, 100401 (2007).
- [26] J. Zhang and T. L. Ho, arXiv:0908.1593.
- [27] D. M. Stamper-Kurn, and M. Ueda, arXiv:1205.1888.
- [28] T. Kawakami *et al.*, arXiv:1204.3177.